Hybrid Photonic−Plasmonic Crystal Nanocavities

Xiaodong Yang,[†,‡,§] Atsushi Ishikawa,[‡,§] Xiaobo Yin,[†,‡] and Xiang Zhang[†,‡,*]

[†]Materials Sciences Division, Lawrence Berkeley National Laboratory, 1 Cyclotron Road, Berkeley, California 94720, United States, and [‡]NSF Nanoscale Science and Engineering Center, 3112 Etcheverry Hall, University of California, Berkeley, California 94720, United States. [§] These authors contributed equally to this work.

Optical micro/nanocavities with both high Q and small V_m are of great importance in the enhancement of light−matter interaction.[1,2] The quality factor Q describes the spectral energy density of the cavity mode, which is proportional to the cavity photon lifetime. The mode volume V_m represents the spatial energy density of the cavity mode, which quantifies the electric field strength per photon. The long photon lifetime and strong light confinement in these high-Q/V_m optical cavities lead to many fundamental studies of optical physics at nanoscale and integrated photonics applications, for example, enhanced spontaneous emission, strong coupling in cavity quantum electrodynamics (QED), enhancement of optical nonlinearities, and optomechanics.[3−6] Although conventional dielectric cavities can be designed to have ultrahigh Q factors, such as microspheres,[7] microtoroids,[8] and photonic crystal cavities,[9] the physical sizes of these cavities cannot be smaller than the wavelength scale in order to confine photon effectively. Therefore, the mode volumes for these dielectric cavities are diffraction-limited and are always larger than the single cubic wavelength $(\lambda/n)^3$.

Surface plasmon polaritons (SPPs) provide a new way to confine electromagnetic (EM) waves beyond the diffraction limit by storing the optical energy in free electron oscillations along the metal−dielectric interface.[10,11] The unique dispersion relation of SPPs supports high wave vectors with ultrashort wavelengths, resulting in different kinds of plasmonic nanocavities with subwavelength mode volumes and metal-loss-limited Q factors, such as plasmonic microdisk resonators,[12] metallic-fin Fabry-Pérot cavities,[13] and metallic-coated nanocavities for miniaturization of lasers.[14−18] With periodic dielectric lattice on the top of the metal layer, plasmonic crystals can be formed to support complete two-dimensional

ABSTRACT We propose a hybrid optical nanocavity consisting of photonic crystals coupled to a metal surface with a nanoscale air gap between. The hybridization of photonic crystal modes and surface plasmons across the gap forms hybrid cavity modes, which are highly confined in the low-loss air gap region. Deep subwavelength mode volume and high quality factor are demonstrated at telecommunication wavelength, resulting in an extremely large Q/V_m ratio of 60 000 λ^{-3}. This new type of high-Q/V_m broad-band hybrid nanocavity opens up opportunities for various applications in enhanced light−matter interactions.

KEYWORDS: optical nanocavity · photonic crystal · surface plasmon polariton · hybrid plasmonic mode

band gaps for SPP manipulation.[19] Plasmonic band gap nanocavities have also been proposed for confining light in deep subwavelength scale.[20] Although plasmonic cavities can achieve deep subwavelength mode volume, their quality factors are always limited by the parasitic loss of metal.

With the advantage of SPPs, a hybrid plasmonic waveguide has been proposed to squeeze optical energy into the nanoscale air gap between the dielectric waveguide and the metal surface.[21] In such a system, both deep subwavelength mode area and low propagation loss have been demonstrated for realizing nanophotonic applications such as nanolasers[22] and optical forces enhancement.[23] The confined optical energy can be boosted by introducing a high-Q optical resonator to enhance the light−matter interactions further.[24] Hybrid plasmonic resonators based on total internal reflection (TIR) have been used to realize the low-threshold plasmonic nanolasers at room temperature.[25] In this paper, we propose a novel hybrid photonic−plasmonic crystal nanocavity by integrating photonic crystal structures into hybrid plasmonic waveguides, as illustrated in Figure 1. On the basis of the periodic variation in the effective index of hybrid mode, a unique hybrid photonic−plasmonic crystal with a transverse magnetic (TM) band gap is formed
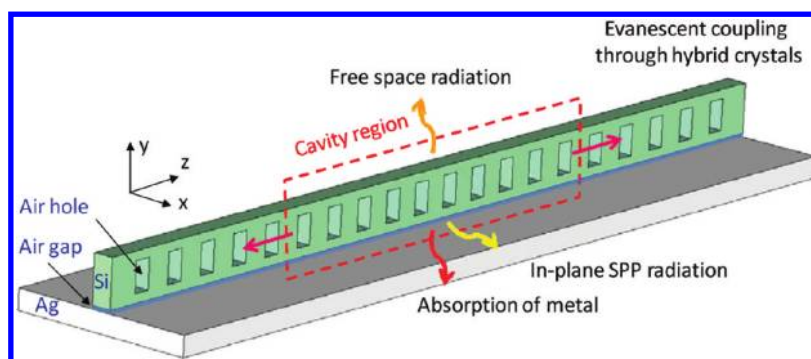
Figure 1. Schematic of the proposed hybrid photonic−plasmonic crystal nanocavity consisting of 10 lattice periods with parabolic variation of lattice constant in the cavity region. The photon loss channels of the hybrid crystal cavity modes include free space radiation, in-plane SPP radiation, evanescent coupling through hybrid crystals, and absorption of metal.
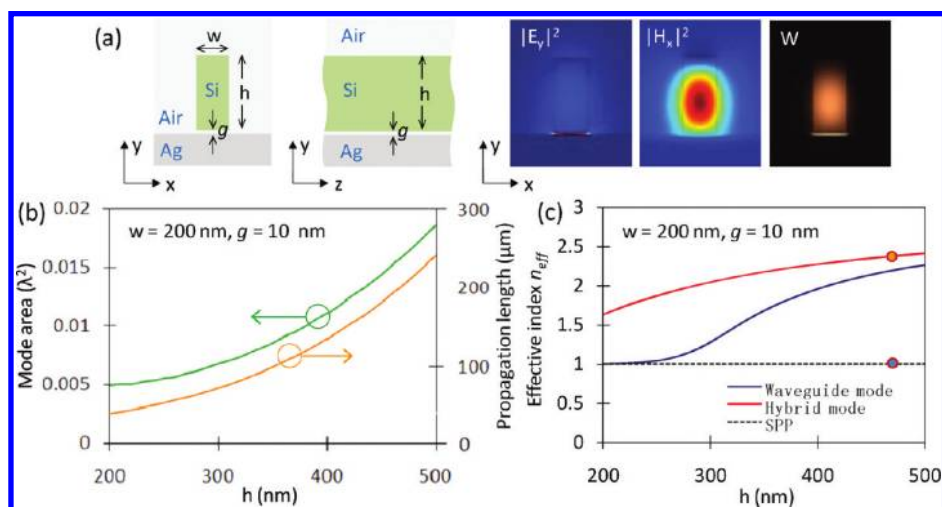

Figure 2. (a) Cross section of the hybrid plasmonic waveguide consisting of a rectangular silicon waveguide (w/h = 200/470 nm) and silver substrate separated by an air gap (g = 10 nm), and the distributions of electric field $|E_y|^2$, magnetic field $|H_x|^2$, and EM energy density W for the fundamental hybrid mode at 200 THz propagating along the z-axis. (b) Mode area A_m and the propagation length L_m of the hybrid mode as a function of the waveguide height h. (c) The h dependence of effective index n_{eff} for the hybrid mode (red curve), bare silicon waveguide mode (blue curve), and bare SPP mode (dotted curve).

at the telecommunication wavelength. One-dimensional hybrid crystal nanocavities having parabolic variation of lattice constant are then designed to realize both high-Q factor and deep subwavelength mode volume V_m, which is due to the strong optical energy concentration in the low-loss air gap region. As shown in Figure 1, the photon loss channels of the hybrid crystal cavity mode include free space radiation, in-plane SPP radiation, evanescent coupling through hybrid crystals, and absorption of metal. We will systematically study the waveguide geometry dependences of radiation Q factor Q_{rad}, absorption Q factor Q_{abs}, V_m, and Q/V_m in order to illustrate the mechanism of the optical confinement in such nanocavities. This new type of high-Q/V_m broadband nanocavity will be of great importance in the enhancement of light−matter interactions, such as cavity QED, nonlinear optics, low-threshold nanoscale lasers, optomechanics, biological sensors,[26,27] and surface-enhanced Raman scattering (SERS).[28−30]

RESULTS AND DISCUSSION

Figure 2a shows the geometry of the hybrid plasmonic waveguide consisting of a rectangular silicon waveguide coupled to a flat silver substrate with a nanoscale air gap g between. In Figure 2a, we also show the distributions of electric field $|E_y|^2$, magnetic field $|H_x|^2$, and EM energy density W for the fundamental hybrid mode at 200 THz propagating along the z-axis. The strong coupling between the silicon waveguide mode and the SPP mode results in the concentration of optical energy inside the low-loss air gap. Figure 2b shows the waveguide height h dependence of the mode area A_m and the propagation length L_m of the hybrid mode with waveguide width w = 200 nm and gap g = 10 nm. The strong optical confinement of the hybrid mode into the nanoscale air gap results in an ultrasmall mode area down to 0.005 λ^2. At the same time, the hybrid mode can travel through a long distance, which is more than 40 μm at 200 THz.
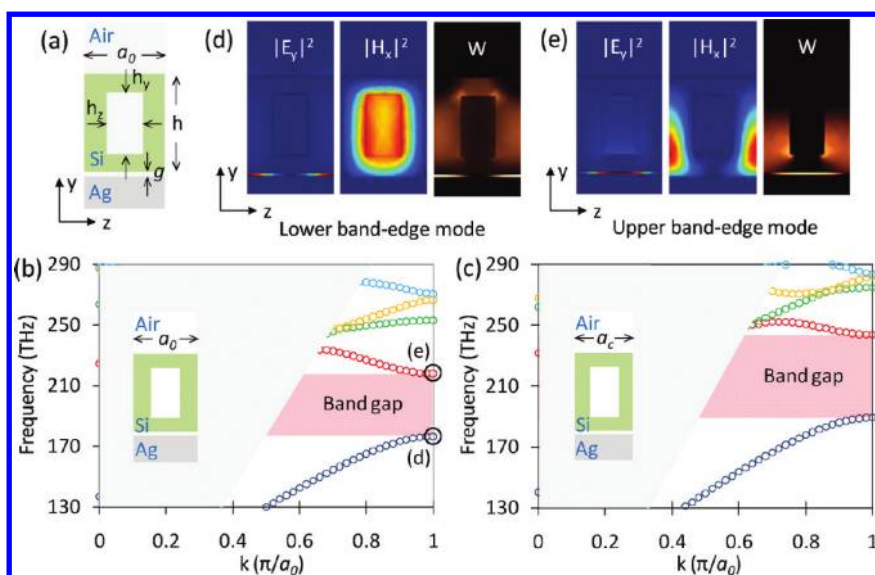
Figure 3. (a) Unit cell of one-dimensional hybrid photonic–plasmonic crystal with a rectangular air hole located inside the silicon waveguide. The TM band structure of the hybrid crystal for the lattice constant (b) $a_0 = 420$ nm and (c) $a_c = 0.9a_0$. The light cone is indicated by the gray region. The corresponding field distributions ($|E_y|^2$, $|H_x|^2$, and W) of lower band-edge mode (d) and upper band-edge mode (e) at the Brillouin zone boundary in (b).

Figure 2c plots the h dependence of effective index n_{eff} for the hybrid mode (red curve), bare silicon waveguide mode (blue curve), and bare SPP mode (dotted curve). Note that the effective index of an optical mode characterizes the phase velocity of the eigenmode popagating along the z direction.[21] For example, when $h = 470$ nm, the effective index of the hybrid mode is $n_{eff} = 2.3735$, which is much larger than the refractive index of the SPP mode at the air–silver interface, where $n_{SPP} = (\varepsilon_m \varepsilon_d/(\varepsilon_m + \varepsilon_d))^{1/2} = 1.0039$. This high index contrast ensures the formation of a hybrid photonic–plasmonic crystal with a TM band gap by introducing photonic crystal structure into the silicon waveguide.

Figure 3a shows the unit cell of a hybrid photonic–-plasmonic crystal by introducing periodic rectangular air holes inside the silicon waveguide along the z-axis. The lattice constant is $a_0 = 420$ nm, and the dimensions of the air hole are $h_y = 0.626h$ and $h_z = 0.4a_0$. In Figure 3b, we show the band structure of the hybrid crystal for TM polarization. A band gap is clearly visible from 176 to 218 THz indicated by the red area, while some higher order modes form the band structure below the light cone (marked by the gray region). Panels d and e of Figure 3 plot the corresponding field distributions ($|E_y|^2$, $|H_x|^2$, and W) of lower band-edge mode (at 176 THz) and upper band-edge mode (at 218 THz) at the Brillouin zone boundary, respectively. The electric field is mostly located in the high effective index region for the lower band-edge mode, whereas the electric field for the upper band-edge mode is concentrated underneath the air hole with low effective index. Figure 3c shows the band structure of the same hybrid crystal but with a smaller lattice constant

$a_c = 0.9a_0$. The band gap will shift to higher frequencies, which is from 189 to 244 THz, due to the reduced effective index as the optical modes have more overlap with air. As a result, by combining these two hybrid crystal structures, the lower band-edge mode with lattice constant a_c lies within the band gap of the unit cell with lattice constant a_0, which will act as the defect cavity mode trapped inside the a_0 lattice. This mechanism of light confinement in mode-gap cavities has been demonstrated to realize ultrahigh Q factor in dielectric photonic crystal cavities.[31−33]

On the basis of the band structure of the hybrid crystal, we have designed a hybrid crystal nanocavity to support the cavity modes highly confined two-dimensionally along both the x and y directions, as shown in Figure 1 and Figure 4a. In order to construct an optical potential well to trap the optical modes along the z-axis, we introduced a parabolic relationship in the lattice constant with the lattice number N from a_0 to $a_c = 0.9a_0$.[32,33] This gradual lattice variation dramatically reduces the mode profile mismatch between the Bloch modes in the cavity and the mirror, so as to address high radiation Q factors. The perturbations of lattice constants span five periods away from the cavity center, so that the cavity region covers 10 lattice periods, as illustrated in Figure 4b. The corresponding lower and upper band-edge frequencies for different lattice number along the z-axis are plotted in Figure 4c. The acceptor-type defect cavity is clearly formed at the Brillouin zone boundary, which supports two eigenmodes in the mode gap. Figure 4d,e illustrates the field distributions of E_y, $|E|^2$, and W for two eigenmodes supported in this cavity, with resonant frequencies of 184 THz for the first order mode ($m = 1$)
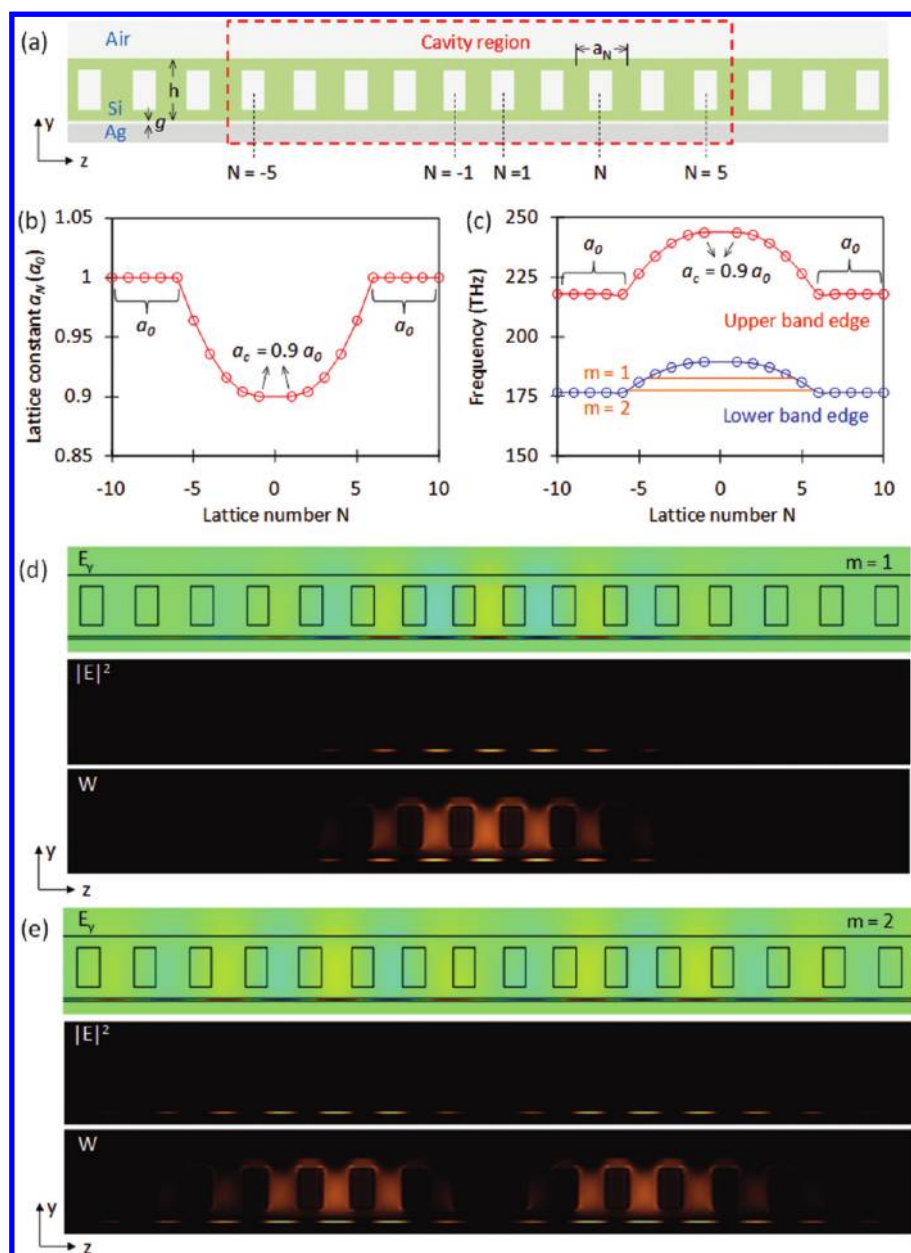
Figure 4. (a) Schematic of the hybrid crystal nanocavity consisting of 10 lattice periods in the cavity region. (b) Lattice constant a_N along the waveguide as a parabolic function of the lattice number N from a_0 to $a_c = 0.9a_0$. (c) Lower and upper band-edge frequencies along the waveguide. The created acceptor-type cavity supports two eigenmodes ($m = 1$ and $m = 2$) inside the mode gap. The corresponding field distributions (E_y, $|E|^2$, and W) for the two eigenmodes (d) $m = 1$ and (e) $m = 2$ of hybrid crystal cavity with $g = 10$ nm.

with even symmetry respect to the $x-y$ plane and 178 THz for the second order mode ($m = 2$) with odd symmetry. The electrical field intensity $|E|^2$ is strongly squeezed inside the low-loss air gap, while most of the EM energy density W is also concentrated inside the gap region. The modes are confined within only several lattice periods in the cavity region along the z-axis. The total quality factors Q_{tot} reach 457 and 338 for the first-order mode and the second-order mode, respectively. $1/Q_{tot} = 1/Q_{rad} + 1/Q_{abs}$, where Q_{rad} is the radiation Q factor and Q_{abs} is the absorption Q factor due to the ohmic loss of the metal. The mode volume V_m is around

2 orders of magnitude smaller than the wavelength cubic, which is 0.0092 $(\lambda/n_{air})^3$ and 0.0122 $(\lambda/n_{air})^3$ for each mode.

Figure 5 shows the dependences of quality factor Q, mode volume V_m, and the Q_{tot}/V_m ratio on the gap separation g for the waveguide with $w = 200$ nm and $h = 470$ nm. For $m = 1$ mode plotted in Figure 5a, as g is increased from 0 to 50 nm, Q_{abs} increases almost linearly because the coupling between the silicon waveguide mode and SPPs is getting weaker so that the energy loss inside the metal is reduced. When $g = 0$, the pure plasmonic crystal cavity mode shown in
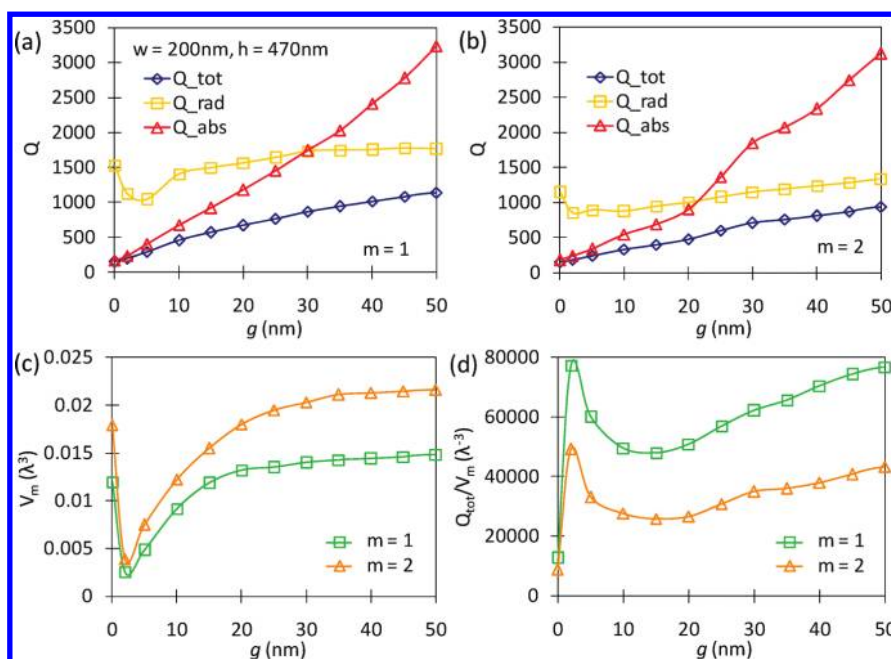
Figure 5. Dependences of quality factors Q_{tot}, Q_{rad}, and Q_{abs} on the gap separation g with $w = 200$ nm and $h = 470$ nm for the two eigenmodes (a) $m = 1$ and (b) $m = 2$. (c) Mode volume V_m and (d) Q_{tot}/V_m ratio as a function of air gap g for the two eigenmodes.
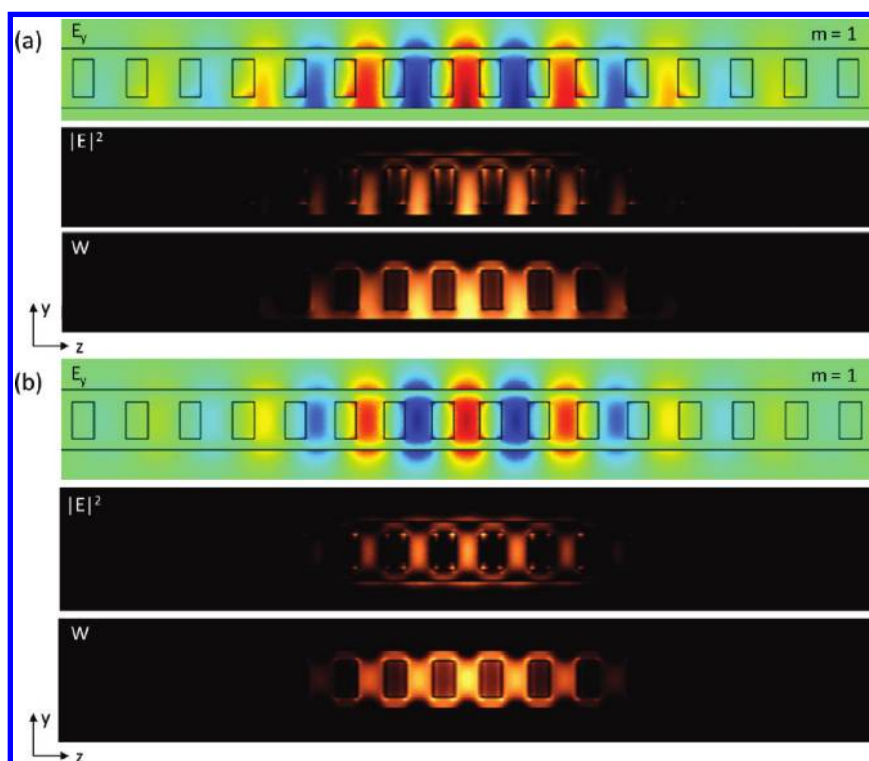

Figure 6. (a) Field distributions (E_y, $|E|^2$, and W) for $m = 1$ mode of pure plasmonic crystal cavity ($g = 0$). (b) Field distributions (E_y, $|E|^2$, and W) for $m = 1$ mode of conventional dielectric photonic crystal cavity ($g = \infty$).

Figure 6a suffers from the largest absorption loss of the metal. On the other hand, Q_{rad} slightly increases for the hybrid cavity mode as g changes from 2 to 50 nm because the free space radiation due to the optical scattering from the air gap and the radiation coupled to the in-plane SPP radiation are slightly reduced as the air gap gets larger. The radiation loss is mostly determined by the hybrid crystal structure and weakly depends on the coupling between the dielectric waveguide mode and the SPP mode, which is limited by

the Q_{rad} of dielectric photonic crystal cavity mode shown in Figure 6b (where $Q_{rad} \sim 1525$). The pure plasmonic crystal cavity mode has a relatively higher Q_{rad} compared to the hybrid crystal cavity mode, due to the absence of the optical scattering from the air gap. Q_{abs} dominates the optical loss when $g < 30$ nm. Q_{tot} gradually increase from 153 to 1140 as the gap varies from 0 to 50 nm. As plotted in Figure 5c, the mode volume V_m for $m = 1$ mode of hybrid crystal cavity can be above 2 orders of magnitude smaller than the wavelength cubic. For example, at $g = 2$ nm, hybrid crystal cavity mode has V_m of 0.0025 $(\lambda/n_{air})^3$. As a comparison, pure plasmonic crystal cavity mode has a large V_m of 0.51 $(\lambda/n_{si})^3$, and dielectric photonic crystal cavity mode also has a similar V_m of 0.64 $(\lambda/n_{si})^3$ because the optical energy is mostly confined in the high-index dielectric structures for both cases, which are above 200 times larger than the mode volume of hybrid crystal cavity mode. As a result, the nanoscale air gap is essential in the proposed system to support the hybrid mode for the deep subwavelength V_m and improved Q_{tot}. The figure of merit for optical cavities

TABLE 1. Lattice Constant a_0, Hole Size h_y and h_z for Different Waveguide Height h in Figure 7

h (nm)	a_0 (nm)	h_y ($\times h$)	h_z ($\times a_0$)
250	730	0.5	0.7
300	650	0.6	0.65
350	570	0.6	0.6
400	490	0.6	0.5
470	420	0.626	0.4

Q_{tot}/V_m ratio is then plotted in Figure 5d. The plasmonic crystal cavity mode has a Q_{tot}/V_m ratio of 300 $(\lambda/n_{si})^{-3}$, and the dielectric photonic crystal cavity mode has 2400 $(\lambda/n_{si})^{-3}$ for $m = 1$ mode, while the Q_{tot}/V_m ratio of hybrid crystal cavity mode is above 48 000 $(\lambda/n_{air})^{-3}$ with a maximum value of 77 000 $(\lambda/n_{air})^{-3}$ at $g = 2$ nm. This ultralarge Q_{tot}/V_m ratio will significantly increase the Purcell factor and enhance the spontaneous emission rate for emitters in the cavity center.[34] The $m = 2$ mode has a lower Q_{rad} because its resonant frequency is close to the lower band edge of the band gap, as shown in Figure 4c, leading to large evanescent coupling through hybrid crystals along the z direction. The mode volume of the $m = 2$ mode is slightly larger than the $m = 1$ mode, due to the broadening of the mode distribution along the z-axis.

Even larger Q_{tot}/V_m ratio can be obtained by tuning the waveguide height h. According to Figure 2c, as h is increased, the effective index n_{eff} for the hybrid mode gets larger (shown in the red curve), leading to lower resonant frequencies of the cavity modes. To systematically study the h dependences of Q and V_m at the same frequency region, we also tuned the lattice constant a_0 and the hole size h_y and h_z for different waveguide height h, as listed in Table 1. Figure 7a plots the calculated band-edge frequencies and the resonant frequencies of two eigenmodes for various waveguide height h with $w = 200$ nm and $g = 10$ nm. Figure 7b–d shows the dependences of Q, V_m, and Q_{tot}/V_m ratio on h for $m = 1$ mode. As h varies from 250 to 470 nm, the effective index gets larger and more optical energy is located inside the dielectric waveguide
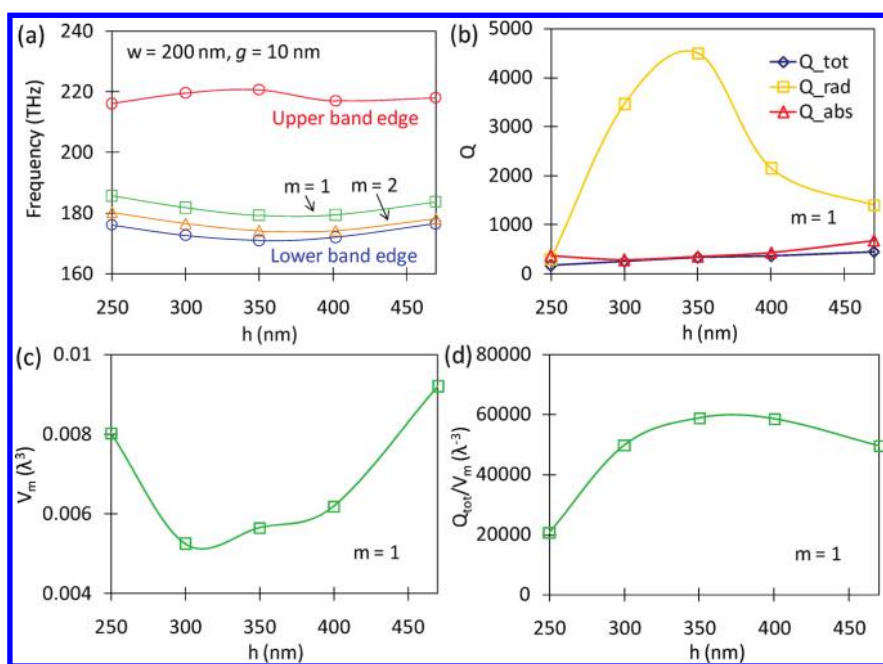

Figure 7. (a) Calculated band-edge frequencies and the resonant frequencies of two eigenmodes for various waveguide height h with $w = 200$ nm and $g = 10$ nm. The dependences of quality factors Q_{tot}, Q_{rad}, and Q_{abs} (b), the mode volume V_m (c), and the Q_{tot}/V_m ratio (d) on h for $m = 1$ mode.

mode, which results in the reduced metal loss and the slight increase of Q_{abs}, as shown in Figure 7b. Q_{rad} reaches its maxima of 4500 at $h = 350$ nm with $a_0 = 570$ nm. Although absorption in the metal always dominates the optical energy loss, Q_{tot} can be as high as 330 at $h = 350$ nm. The strong optical confinement gives a deep sub-wavelength mode volume of 0.0056 $(\lambda/n_{air})^3$ at $h = 350$ nm, resulting in an extremely large Q_{tot}/V_m of 60 000 $(\lambda/n_{air})^{-3}$, as shown in Figure 7c,d. The enhancement of the spontaneous emission rate of a radiating dipole into the cavity mode with a perfect spatial and spectral matching, compared to the emission rate in the bulk material, can be described by the Purcell factor[34,35]

$$F_P = \frac{3}{4\pi^2}\left(\frac{\lambda}{n}\right)^3\left(\frac{Q_{tot}}{V_m}\right)$$

where n is the index of refraction at the field intensity maximum. Our proposed system can achieve $F_p \approx 4560$ for the cavity having Q_{tot}/V_m of 60 000 $(\lambda/n_{air})^{-3}$ and $n = n_{air}$, with the waveguide geometry of $w = 200$ nm, $h = 350$ nm, and $g = 10$ nm. The Q_{tot} can be increased furthermore by reducing the temperature, where the damping collision frequency of the free electrons in the metal is decreased so that a larger Purcell factor may be achieved.[14−16] SERS signal from a single molecule can also be significantly improved with the current hybrid crystal nanocavity since the enhancement of both the incoming pump light and the scattered Stokes signal are proportional to Q_{tot}^2/V_m and a giant increase of the Raman scattering cross section for the molecule can be achieved.[28]

CONCLUSION

We have proposed a hybrid photonic−plasmonic crystal nanocavity to achieve both deep subwavelength mode volume and high quality factor. High quality factor Q_{tot} of 330 and deep subwavelength mode volume V_m of 0.0056 λ^3 are demonstrated at telecommunication wavelength. The calculated Purcell factor is as high as 4560 with an extremely large Q_{tot}/V_m of 60 000 λ^{-3}. This new type of broad-band hybrid nanocavity can be used to realize many exciting applications in enhanced light−matter interactions, such as cavity QED, nanolasers, optomechanics, biological sensors, and SERS.

METHODS

Numerical Simulations. The calculations are performed using the finite-element method (FEM) software package (COMSOL) with $n_{si} = 3.5$ and the empirical value for n_{Ag} based on the Drude model,[36] where $\varepsilon_{Ag} = \varepsilon_\infty - \omega_p^2/(\omega^2 - i\omega\gamma)$ with background dielectric constant $\varepsilon_\infty = 5.0$, plasma frequency $\omega_p = 1.38 \times 10^{16}$ rad/s, and collision frequency $\gamma = 5.07 \times 10^{13}$ rad/s. The mode area for the hybrid plasmonic waveguide is calculated from $A_m = W_m/\max[W(\vec{r})]$, where W_m is the integrated EM energy over the entire space $W_m = \int\int W(\vec{r})d^2r$, and $W(\vec{r})$ is the local EM energy density at the position $\vec{r}$, taking into account the strongly dispersive property of silver,[12] such that

$$W(\vec{r}) = \frac{1}{2}\left[\mathrm{Re}\left[\frac{d(\omega\varepsilon)}{d\omega}\right]|\vec{E}(\vec{r})|^2 + \mu|\vec{H}(\vec{r})|^2\right]$$

The mode volume of the hybrid photonic−plasmonic nanocavity is calculated as

$$V_m = \frac{W_m}{\max[W(\vec{r})]} = \frac{1}{\max[W(\vec{r})]}\int\int\int W(\vec{r})d^3r$$

The Q factors of the cavity modes are calculated from the formula $Q = f_R/\Delta f$, with the resonance frequency f_R and the full width at half-maximum (fwhm) of the resonance intensity spectrum Δf, which are calculated from the full wave simulations using the finite-difference time-domain method (CST Microwave Studio). The radiation Q factor can be calculated and separated from the absorption Q factor due to the metal loss by removing the imaginary part of the permittivity of silver.

REFERENCES AND NOTES

1. Yamamoto, Y.; Slusher, R. E. Optical Processes in Micro-cavities. *Phys. Today* **1993,** *46*, 66–73.

2. Vahala, K. J. Optical Microcavities. *Nature* **2003,** *424*, 839–846.

3. Noda, S.; Fujita, M.; Asano, T. Spontaneous-Emission Control by Photonic Crystals and Nanocavities. *Nat. Photonics* **2007,** *1*, 449–458.

4. Yoshie, T.; Scherer, A.; Hendrickson, J.; Khitrova, G.; Gibbs, H. M.; Rupper, G.; Ell, C.; Shchekin, O. B.; Deppe, D. G. Vacuum Rabi Splitting with a Single Quantum Dot in a Photonic Crystal Nanocavity. *Nature* **2004,** *432*, 200–203.

5. Soljacic, M.; Joannopoulos, J. D. Enhancement of Nonlinear Effects Using Photonic Crystals. *Nat. Mater.* **2004,** *3*, 211–219.

6. Kippenberg, T. J.; Vahala, K. J. Cavity Optomechanics: Back-Action at the Mesoscale. *Science* **2008,** *321*, 1172.

7. Spillane, S. M.; Kippenberg, T. J.; Vahala, K. J. Ultralow-Threshold Raman Laser Using a Spherical Dielectric Micro-cavity. *Nature* **2002,** *415*, 621–623.

8. Armani, D. K.; Kippenberg, T. J.; Spillane, S. M.; Vahala, K. J. Ultra-High-Q Toroid Microcavity on a Chip. *Nature* **2003,** *421*, 925–928.

9. Akahane, Y.; Asano, T.; Song, B. S.; Noda, S. High-Q Photonic Nanocavity in a Two-Dimensional Photonic Crystal. *Nature* **2003,** *425*, 944–947.

10. Barnes, W. L.; Dereux, A.; Ebbesen, T. W. Surface Plasmon Subwavelength Optics. *Nature* **2003,** *424*, 824–830.

11. Schuller, J. A.; Barnard, E. S.; Cai, W.; Jun, Y. C.; White, J. S.; Brongersma, M. L. Plasmonics for Extreme Light Concentration and Manipulation. *Nat. Mater.* **2010,** *9*, 193.

12. Min, B.; Ostby, E.; Sorger, V.; Ulin-Avila, E.; Yang, L.; Zhang, X.; Vahala, K. High-Q Surface-Plasmon-Polariton Whispering-Gallery Microcavity. *Nature* **2009,** *457*, 455–458.

13. Sorger, V. J.; Oulton, R. F.; Yao, J.; Bartal, G.; Zhang, X. Plasmonic Fabry-Pérot Nanocavity. *Nano Lett.* **2009,** *9*, 3489.

14. Hill, M. T.; Oei, Y.-S.; Smalbrugge, B.; Zhu, Y.; de Vries, T.; van Veldhoven, P. J.; van Otten, F. W. M.; Eijkemans, T. J.; Turkiewicz, J. P.; de Waardt, H.; Geluk, E. J.; Kwon, S.-H.; Lee, Y.-H.; Nötzel, R.; Smit, M. K. Lasing in Metallic-Coated Nanocavities. *Nat. Photonics* **2007,** *1*, 589–594.

15. Seo, M.; Kwon, S.; Ee, H.-S.; Park, H.-G. Full Three-Dimensional Subwavelength High-Q Surface-Plasmon-Polariton Cavity. *Nano Lett.* **2009,** *9*, 4078.

16. Kwon, S.; Kang, J.; Seassal, C.; Kim, S.; Regreny, P.; Lee, Y. H.; Lieber, C. M.; Park, H.-G. Subwavelength Plasmonic Lasing from a Semiconductor Nanodisk with Silver Nanopan Cavity. *Nano Lett.* **2010,** *10*, 3679–3683.

17. Nezhad, M. P.; Simic, A.; Bondarenko, O.; Slutsky, B.; Mizrahi, A.; Feng, L.; Lomakin, V.; Fainman, Y. Room-Temperature Subwavelength Metallo-Dielectric Lasers. *Nat. Photonics* **2010,** *4*, 395–399.

18. Yu, K.; Lakhani, A.; Wu, M. C. Subwavelength Metal-Optic Semiconductor Nanopatch Lasers. *Opt. Express* **2010,** *18*, 8790–8799.

19. Feng, L.; Lu, M. H.; Lomakin, V.; Fainman, Y. Plasmonic Photonic Crystal with a Complete Band Gap for Surface Plasmon Polariton Waves. *Appl. Phys. Lett.* **2008,** *93*, 231105.

20. Kim, M.; Lee, S. H.; Choi, M.; Ahn, B. H.; Park, N.; Lee, Y. H.; Min, B. Low-Loss Surface-Plasmonic Nanobeam Cavities. *Opt. Express* **2010,** *18*, 11089–11096.

21. Oulton, R. F.; Sorger, V.; Genov, D. A.; Pile, D. F. P.; Zhang, X. A Hybrid Plasmonic Waveguide for Subwavelength Confinement and Long-Range Propagation. *Nat. Photonics* **2008,** *2*, 496.

22. Oulton, R. F.; Sorger, V. J.; Zentgraf, T.; Ma, R.-M.; Gladden, C.; Dai, L.; Bartal, G.; Zhang, X. Plasmon Lasers at Deep Subwavelength Scale. *Nature* **2009,** *461*, 629–632.

23. Yang, X.; Liu, Y.; Oulton, R. F.; Yin, X.; Zhang, X. Optical Forces in Hybrid Plasmonic Waveguides. *Nano Lett.* **2011,** *11*, 321–328.

24. Xiao, Y.-F.; Li, B.-B.; Jiang, X.; Hu, X.; Li, Y.; Gong, Q. High Quality Factor, Small Mode Volume, Ring-Type Plasmonic Microresonator on a Silver Chip. *J. Phys. B: At., Mol. Opt. Phys.* **2010,** *43*, 035402.

25. Ma, R.-M.; Oulton, R. F.; Sorger, V. J.; Bartal, G.; Zhang, X. Room Temperature Sub-Diffraction-Limited Plasmon Laser by Total Internal Reflection. *Nat. Mater.* **2011,** *10*, 110.

26. Sun, C.; Su, K.-H.; Valentine, J.; Rosa-Bauza, Y. T.; Ellman, J. A.; Elboudwarej, O.; Mukherjee, B.; Craik, C. S.; Shuman, M. A.; Chen, F. F.; Zhang., X. Time-Resolved Single-Step Protease Activity Quantification Using Nanoplasmonic Resonator Sensors. *ACS Nano* **2010,** *4*, 978–984.

27. McPhillips, J.; Murphy, A.; Jonsson, M. P.; Hendren, W. R.; Atkinson, R.; Hook, F.; Zayats, A. V.; Pollard, R. J. High-Performance Biosensing Using Arrays of Plasmonic Nanotubes. *ACS Nano* **2010,** *4*, 2210–2216.

28. Maier, S. A. Plasmonic Field Enhancement and SERS in the Effective Mode Volume Picture. *Opt. Express* **2006,** *14*, 1957–1964.

29. Lee, S. Y.; Hung, L.; Lang, G. S.; Cornett, J. E.; Mayergoyz, I. D.; Rabin, O. Dispersion in the SERS Enhancement with Silver Nanocube Dimers. *ACS Nano* **2010,** *4*, 5763–5772.

30. Gehan, H.; Fillaud, L.; Chehimi, M. M.; Aubard, J.; Hohenau, A.; Felidj, N.; Mangeney, C. Thermo-Induced Electromagnetic Coupling in Gold/Polymer Hybrid Plasmonic Structures Probed by Surface-Enhanced Raman Scattering. *ACS Nano* **2010,** *4*, 6491–6500.

31. Song, B.-S.; Noda, S.; Asano, T.; Akahane, Y. Ultra-High-*Q* Photonic Double-Heterostructure Nanocavity. *Nat. Mater.* **2005,** *4*, 207.

32. Notomi, M.; Kuramochi, E.; Taniyama, H. Ultrahigh-*Q* Nanocavity with 1D Photonic Gap. *Opt. Express* **2008,** *16*, 11095.

33. Chan, J.; Eichenfield, M.; Camacho, R.; Painter, O. Optical and Mechanical Design of a `Zipper' Photonic Crystal Optomechanical Cavity. *Opt. Express* **2009,** *17*, 3802.

34. Robinson, J. T.; Manolatou, C.; Chen, L.; Lipson, M. Ultra-small Mode Volumes in Dielectric Optical Microcavities. *Phys. Rev. Lett.* **2005,** *95*, 143901.

35. Purcell, E. M. Spontaneous Emission Probabilities at Radio Frequencies. *Phys. Rev.* **1946,** *69*, 681.

36. Johnson, P. B.; Christie, R. W. Optical Constants of the Noble Metals. *Phys. Rev. B* **1972,** *6*, 4370.

射 频 和 天 线 设 计 培 训 课 程 推 荐

易迪拓培训(www.edatop.com)由数名来自于研发第一线的资深工程师发起成立，致力并专注于微波、射频、天线设计研发人才的培养；我们于 2006 年整合合并微波 EDA 网(www.mweda.com)，现已发展成为国内最大的微波射频和天线设计人才培养基地，成功推出多套微波射频以及天线设计经典培训课程和 ADS、HFSS 等专业软件使用培训课程，广受客户好评；并先后与人民邮电出版社、电子工业出版社合作出版了多本专业图书，帮助数万名工程师提升了专业技术能力。客户遍布中兴通讯、研通高频、埃威航电、国人通信等多家国内知名公司，以及台湾工业技术研究院、永业科技、全一电子等多家台湾地区企业。

易迪拓培训课程列表：http://www.edatop.com/peixun/rfe/129.html

射频工程师养成培训课程套装

该套装精选了射频专业基础培训课程、射频仿真设计培训课程和射频电路测量培训课程三个类别共 30 门视频培训课程和 3 本图书教材；旨在引领学员全面学习一个射频工程师需要熟悉、理解和掌握的专业知识和研发设计能力。通过套装的学习，能够让学员完全达到和胜任一个合格的射频工程师的要求…

课程网址：http://www.edatop.com/peixun/rfe/110.html

ADS 学习培训课程套装

该套装是迄今国内最全面、最权威的 ADS 培训教程，共包含 10 门 ADS 学习培训课程。课程是由具有多年 ADS 使用经验的微波射频与通信系统设计领域资深专家讲解，并多结合设计实例，由浅入深、详细而又全面地讲解了 ADS 在微波射频电路设计、通信系统设计和电磁仿真设计方面的内容。能让您在最短的时间内学会使用 ADS，迅速提升个人技术能力，把 ADS 真正应用到实际研发工作中去，成为 ADS 设计专家…

课程网址：　http://www.edatop.com/peixun/ads/13.html

HFSS 学习培训课程套装

该套课程套装包含了本站全部 HFSS 培训课程，是迄今国内最全面、最专业的 HFSS 培训教程套装，可以帮助您从零开始，全面深入学习 HFSS 的各项功能和在多个方面的工程应用。购买套装，更可超值赠送 3 个月免费学习答疑，随时解答您学习过程中遇到的棘手问题，让您的 HFSS 学习更加轻松顺畅…

课程网址：http://www.edatop.com/peixun/hfss/11.html